RSC Advances

PAPER

View Article Online
View Journal | View Issue

Cite this: *RSC Adv.*, 2026, **16**, 13982

Mussel-inspired silica, strontium, and fluoride-doped hydroxyapatite/BMP-2 composite coating: a new strategy to enhance the bioactivity of zirconia implants

Jing Li,†[a] Rongzhu Gao,†[a] Tong Chen,†[a] Kehan Deng,[b] Zhao Dai,[c] Jianyong Gao*[a] and Gang Tian*[a]

Zirconium dioxide (ZrO_2, zirconia) is widely regarded as an ideal material for dental implants due to its superior aesthetics, biocompatibility, and mechanical performance. However, its bioinert nature limits its clinical potential, leading to poor integration between the implant and surrounding bone tissue. Inspired by mussel adhesive proteins, we constructed a composite coating of silicon, strontium, and fluoride-doped hydroxyapatite (with theoretical dopant concentrations) and bone morphogenetic protein-2 (BMP-2) on zirconia surfaces using a polydopamine-assisted immersion method. The surfaces were pre-treated using a chemical deposition method to enhance the coating adhesion. The modified surfaces were characterized using field emission scanning electron microscopy, X-ray diffraction, Fourier-transform infrared spectroscopy, X-ray photoelectron spectroscopy, and an optical contact angle meter. The composite coating significantly promoted the attachment and proliferation of pre-osteoblastic MC3T3-E1 cells. After 14 days, cells on the coated surfaces exhibited higher mRNA expression of runt-related transcription factor-2 (Runx2), alkaline phosphatase (ALP), and osteocalcin (OCN). *In vitro* ALP staining and alizarin red S staining showed enhanced ALP activity and calcium nodule formation. Surface pre-treatment significantly improved coating adhesion strength. This bioactive modification, with the dopant concentrations of Si/Sr/F in hydroxyapatite being theoretical design values, enhances zirconia implant bioactivity, offering a novel approach to improve clinical outcomes.

Received 22nd December 2025
Accepted 4th March 2026

DOI: 10.1039/d5ra09896c

rsc.li/rsc-advances

1 Introduction

Yttria-stabilized tetragonal zirconia polycrystals (Y-TZP) are widely used in the dental field as a ceramic material due to their excellent mechanical properties, aesthetic appearance, and superior biocompatibility. In particular, zirconia has unique characteristics that mimic the appearance of natural teeth and reduce peri-implant inflammatory responses.[1] Despite the excellent mechanical properties of zirconia, including high strength and good fracture toughness, challenges exist in osseointegration due to the bioinert nature and lack of direct bone-binding of zirconia.[2,3] Zirconia typically requires more surface modifications compared to titanium to promote the adhesion, proliferation, and differentiation of osteoblasts and fibroblasts, which facilitates bone integration on the implant surface and adaptation to the surrounding soft tissue of the implant.[4,5] According to the current literature,[1,6,7] modifying the surface of zirconia is a key means of enhancing its osseointegration ability. Various physicochemical methods have been used to alter zirconia surface characteristics to improve early and late bone-implant integration. For example, Gao *et al.*[8] established a unique micro/nanostructured porous zirconia through dry pressing with a pore-forming agent, followed by hydrofluoric acid etching (POROHF). Unetched porous zirconia, sandblasted and acid-etched zirconia, and sintered zirconia surfaces served as control groups. After seeding human bone marrow mesenchymal stem cells (hBMSCs) onto these four zirconia surfaces, the POROHF surface showed the highest cell affinity and extension rate, and the best osteogenic phenotype. Additionally, the POROHF surface promoted angiogenesis of hBMSCs. Importantly, the POROHF group demonstrated the most significant bone matrix development *in vivo*. For example, Huang *et al.* developed coatings with antibacterial, anti-inflammatory, and pro-angiogenic bone formation abilities through techniques such as layer-by-layer self-assembly, phase change, hydrothermal reaction, and spin coating.[9–13] Recent studies have further demonstrated that co doping strategies in hydroxyapatite (such as Sr/F/Si) and growth factors such as

[a]*Department of Stomatology, Changhai Hospital of Shanghai, The First Affiliated Hospital of Naval Medical University, Shanghai 200433, China. E-mail: gaojianyong2024@163.com*
[b]*Southern Theater Command Navy Second Hospital, China*
[c]*The 903 Hospital of the Chinese People's Liberation Army, China*
† Jing Li, Rongzhu Gao and Tong Chen contributed equally to this work.

BMP-2, when combined with various biomaterials, may significantly enhance bone integration through synergistic biological activity.[14,15] These studies all indicate that different surface modification methods can significantly improve the comprehensive performance of biomaterials, providing diverse solutions for addressing implant-related problems. These results indicate that, despite the bioinertness of zirconia as a challenge, appropriate surface modifications can transform zirconia from a "bioinert" surface to a "bioactive" multifunctional surface, achieving bone integration effects comparable to those of titanium implants. Although various methods exist for surface treatment, including laser surface treatment, chemical corrosion, sandblasting, and polishing, these methods may trigger the transformation of zirconia ceramics from the tetragonal phase to the monoclinic phase (t–m), thereby altering their mechanical properties.[16,17] Inspired by the adhesion of mussels to surfaces, polydopamine (PDA) coatings can be formed through dopamine self-polymerization under mild reaction conditions through a simple experimental procedure[18] and can be used to modify various surfaces, including the surfaces of dental implants.[19]

Hydroxyapatite is the most widely used biomaterial in bone tissue engineering, and an inorganic composition similar to that of natural bone, it exhibits good biocompatibility and osteoinductivity.[20] Hydroxyapatite is rich in Ca and P ions, which may promote the formation of apatite crystals.[21] However, the ability of hydroxyapatite to promote bone regeneration is limited, in part because bone tissue is not only composed of calcium and phosphorus elements, but also contains a variety of trace elements, such as Zn^{2+}, Sr^{2+}, Mg^{2+}, Fe^{2+}, Na^{+}, Cl^{-}, F^{-}, K^{+}, Si^{4+}, and Cr^{2+}.[22,23] Therefore, co-doping with multiple trace elements is needed to further enhance the osteogenic capacity of hydroxyapatite. Silicon is an important trace element in the body, and studies have shown that incorporating silicon into hydroxyapatite can significantly improve its crystallinity and growth rate. In particular, silicon doping can promote the growth of hydroxyapatite along the *c*-axis to form large-sized nanorod structures that more effectively combine with bone tissue, thereby enhancing bone healing and integration.[24,25] Strontium is believed to improve the antisolvent properties and bioactivity of hydroxyapatite. Studies have shown that incorporating strontium into hydroxyapatite enhanced its mechanical strength and bioactivity, while promoting the process of bone integration by improving the balance of bone formation and resorption.[26] Fluoride interacts with the hydroxyl ions in hydroxyapatite to form fluorapatite, which promotes bone mineralization of the biomaterial while enhancing its acid resistance, antibacterial properties, and stability.[25,27] Bone morphogenetic protein-2 (BMP-2) is a member of the transforming growth factor-β (TGF-β) superfamily that activates specific signaling pathways to promote osteogenic differentiation of bone marrow mesenchymal stem cells.[28,29] Studies have shown[30] that BMP-2 applied to the surface of implants significantly enhanced the osseointegration capability of the implants. Zirconia with surface modifications has demonstrated faster osseointegration than untreated surfaces. However, a consensus on the types of surface treatment and subsequent surface morphology that enhance osseointegration has not yet been formed. Therefore, more research is needed to further explore the best methods for zirconia surface treatment to achieve more effective osseointegration and long-term stability of implants.

Inspired by mussel adhesion, in this study we developed a novel method of modifying the zirconia surfaces with PDA and then deposited hydroxyapatite co-doped with Si, Sr, and F, combined with BMP-2 to enhance osseointegration. The modified zirconia surface coatings were systematically characterized, including through physical and chemical property analyses and coating adhesion strength testing, to assess the changes induced by the modification. Finally, the biocompatibility and osteogenic potential of this composite coating were evaluated.

2 Materials and methods

2.1 Material preparation

2.1.1 Preparation of the nano-zirconia coating on the zirconia surface. In this study, zirconia discs (Alloytek, China) with a diameter of 6 mm and a thickness of 3 mm were polished with 600-grit silicon carbide abrasive paper (SAK 600-CW, Mipox, Japan) to obtain ZrO_2 substrates (Z). The zirconia discs were then ultrasonically cleaned in distilled water, acetone, and anhydrous ethanol for 10 minutes and dried. Each zirconia disk was immersed in 1 mL of a 2 mg mL^{-1} dopamine solution (Adamas-beta, China) (prepared with 10 mM Tris–HCl buffer solution, pH 8.5) and reacted in a constant temperature incubator shaker at 37 °C and 150 rpm for 24 hours. After the reaction, the disks were rinsed three times with deionized water and then immersed in 1 mL of an 8 mM $Zr(SO_4)_2$ solution (prepared with 0.2 M HCl) in a constant temperature shaking incubator at 50 °C and 150 rpm for 24 hours. Finally, the disks were cleaned with deionized water in an ultrasonic cleaner for 5 minutes, dried, and calcined in a high-temperature box furnace (SG-XL 1400, China) at 900 °C for 10 minutes to obtain the $nZrO_2$ (N) disc samples.

2.1.2 Preparation of the mHA/BMP-2 composite coating on the zirconia surface. Referring to the previous research results of our group,[31] multi-doped hydroxyapatite (mHA) with the same content of silicon, strontium, and fluorine as that of natural bone apatite was prepared by hydrothermal synthesis, the concentrations of the doped elements in mHA used in this study were based on theoretical design values (reported in parts per million, ppm) without verification by direct elemental quantitative analysis, as follows: silicon (Si): 56 ppm; strontium (Sr): 87 ppm; fluorine (F): 190 ppm. The $nZrO_2$ was then divided into two groups. One group was incubated in a 2 mg mL^{-1} DA–Tris solution for 24 hours and the other also with a 4 mg mL^{-1} mHA–Tris solution for 24 hours to produce $nZrO_2$–PDA (ND) and $nZrO_2$–PDA–mHA (NDm), respectively. As a control for testing the coating adhesion strength, the PDA/mHA coating was prepared on ZrO_2 disks without nano-zirconia coating using the same manner to produce ZrO_2–PDA–mHA (ZDm). Finally, after the completion of nano-zirconia coating sintering and PDA/mHA coating preparation, the autoclaved $nZrO_2$–PDA

and $nZrO_2$–PDA–mHA samples were soaked in a sterile BMP-2 solution (5 μg mL^{-1}) at 4 °C for 1 hour to produce the samples $nZrO_2$–PDA–BMP2 (NDB) and $nZrO_2$–PDA–mHA–BMP2 (NDmB), respectively.

2.2 Characterization of the mHA/BMP-2 composite coating

Samples Z, N, ND, NDm, NDB, and NDmB were examined using field emission scanning electron microscopy (FE-SEM, S-4800, Japan) and X-ray diffractometer (XRD, Ultima IV, Japan), and by using an automatic optical dynamic contact angle meter (SL200C, USA). A PDA coating powder and potassium bromide powder were ground and mixed uniformly at a mass ratio of 1 : 100 and pressed into thin sheets, which were analyzed using Fourier-transform infrared spectroscopy (FTIR, IRAffinity-1, Japan). X-ray photoelectron spectroscopy (XPS, ESCALAB 250, USA) was used to identify and analyze the chemical elements on the surface of the NDmB sample. Ultrasonication tests were used to determine the adhesion strength between the surface coating and the substrate of the N, NDm, and ZDm samples.[32] The samples were immersed in deionized water and subjected to ultrasonication (53 kHz, ≈150 W cm^{-2}, Kudos Science, China) for 10 min. The mass of each sample was measured before (M_1) ultrasonication. After ultrasonication, the samples were thoroughly rinsed with deionized water, dried in a vacuum oven at 37 °C for 24 hours, and then weighed again (M_2) using a precision microbalance (MSA6.6S-000-DM, Sartorius, Germany, readability 1 μg). The coating adhesion strength was quantitatively assessed by calculating the percentage of mass loss: Mass loss (%) = $[(M_1 - M_2)/M_1] \times 100\%$. Correspondingly, the coating retention rate was calculated as: Retention (%) = $[M_2/M_1] \times 100\%$. This experiment was repeated five times for each group.

2.3 Cell compatibility assessment

2.3.1 Cell culture. Mouse pre-osteoblast cells (MC3T3-E1) used in this experiment were purchased from the Cell Bank of the Chinese Academy of Sciences. The complete culture medium was prepared by adding 10% fetal bovine serum (Gibco, Australia) and 1% penicillin-streptomycin (Beyotime, China) to α-MEM medium (Hyclone, USA). Cells were cultured in a constant temperature cell incubator (Sanyo, Japan) at 37 °C with 5% CO_2, and the complete culture medium was refreshed every two days. When the cells became 90% confluent, they were observed under a microscope and passaged at a ratio of 1 : 2 using 0.25% trypsin–EDTA (Gibco) for 3 min at 37 °C.

2.3.2 *In vitro* cytotoxicity test. The six (Z, N, ND, NDm, NDB, and NDmB) samples were placed in a 24-well plate with 1 mL of complete culture medium as an extraction medium and incubated in a constant temperature shaking incubator at 37 °C for 24 hours. The extracts were collected for later use. MC3T3-E1 cells were seeded in a 96-well plate at a concentration of 6×10^4 cells per mL and incubated at 37 °C and 5% CO_2 for 24 hours. The cells were washed three times with a phosphate buffered saline solution, and 150 μL of extracts with a gradient of concentrations was added to the cells. The cells were incubated at 37 °C and 5% CO_2 for 24 hours. A CCK-8 assay kit was used to quantitatively determine the number of cells in each group. The absorbance at 450 nm was measured using a microplate reader (Thermo Scientific Multiskan FC, China), and the results were statistically analyzed. Each group had six parallel experimental wells, and the experiment was repeated three times.

2.3.3 Cell adhesion and spreading experiment. Cells adhering to the sample surface were fluorescently stained with phalloidin and DAPI, and then observed and photographed under an inverted fluorescence microscope (OLYMPUS, Japan). A Cell Counting Kit-8 (CCK-8) kit (Beyotime, China) was used to determine the number of cells adhering to each sample. The absorbance was measured at 450 nm using a microplate reader and the results were statistically analyzed.

2.3.4 Cell proliferation experiment. Cell proliferation on the surface of each sample was observed using FE-SEM. Sterilized samples from each of the six groups were placed in a 24-well plate, and 1 mL of a MC3T3-E1 cell suspension at a concentration of 2×10^4 cells per mL was added to each well. After culturing for 1, 4, and 7 days, the sample discs from each group were removed and placed in new 24-well plates. After the samples were washed and underwent dehydration treatment, they were observed and photographed using FE-SEM. The number of cells in each group at 1, 4, 7, and 10 days was determined using a CCK-8 kit. The absorbance at 450 nm was measured using a microplate reader, and the results were statistically analyzed.

2.4 Osteogenic differentiation test

2.4.1 Alkaline phosphatase (ALP) activity assay. The ALP activity of cells cultured on the different samples was measured using an ALP assay kit (Beyotime, China) after 4, 7, and 10 days (OD value). Linear fitting (with a requirement of $r \geq 0.99$) was used to calculate the sample ALP activity. A BCA protein concentration assay kit (Beyotime, China) was used to measure the total protein content in the lysate supernatant. The ALP activity was normalized. The results were statistically analyzed. Tests were performed in triplicate with $n = 6$ independent samples per group.

2.4.2 Osteogenic-related gene expression assay. The sterilized sample discs (of the six different treatments) were placed directly in a 24-well plate, and 1 mL of an MC3T3-E1 cell suspension at a concentration of 1.5×10^4 cells per mL was added to each well and incubated at 37 °C and 5% CO_2 for 14 days. Total RNA was extracted from the cells cultured on the samples using TRIzol reagent (Invitrogen Life Technologies), and then converted to cDNA using PrimeScript RT master mix (Takara). PCR analysis was performed using a StepOne real-time PCR system (Applied Biosystems), with mouse GAPDH as the internal reference gene,

Table 1 Primer sequence used for real time quantitative PCR

Gene	Sequence
Runx2	Forward: ATTGCAGGCTTCGTGGTTGAGG
	Reverse: TGGCTGTATGGTGAGGCTGGTAG
ALP	Forward: CACGGCGTCCATGAGCAGAAC
	Reverse: CAGGCACAGTGGTCAAGGTTGG
OCN	Forward: GCTCGGCTTTGGCTGCTCTC
	Reverse: AGCTGCTGTGACATCCATACTTGC

and the relative expression of the osteogenic-related genes Runx2, ALP, and OCN was analyzed. Experiments repeated three times with $n = 4$ biological replicates. The primer sequences of the target genes are shown in Table 1.

The PCR reaction system was prepared according to the instructions of TB Green Premix Ex Taq (Takara, Japan). The relative expression of each target gene was calculated using the $\Delta\Delta C_t$ method, and the results were statistically analyzed.

2.4.3 ***In vitro*** **mineralization assay (alizarin red S staining).** Cells were cultured by seeding sterilized samples from the six groups in a 24-well plate with 1 mL of a well-grown MC3T3-E1 cell suspension at a concentration of 1.5×10^4 cells per mL. The seeded cell culture plates were incubated in a constant temperature incubator at 37 °C with 5% CO_2 for 14 days before subsequent testing. After culturing, the samples were stained with alizarin red S (Solarbio, China) stain, and then observed and photographed under an inverted microscope.

2.5 Statistical analysis

Data were analyzed using IBM SPSS Statistics V21.0 software, and graphs were plotted using Origin Pro8 software. Quantitative data are expressed as the mean ± standard deviation. The results of the cytotoxicity test were analyzed using multifactorial analysis of variance. The cell adhesion and spreading, cell proliferation, and ALP activity results were analyzed using repeated measures analysis of variance. The osteogenic-related gene expression results were analyzed using one-way analysis of variance. All *post hoc* pairwise comparisons were performed using the Least-Significant Difference (LSD) test, with $P < 0.05$ indicating a statistically significant difference.

3 Results

3.1 Material surface analysis

A method was developed to form the PDA/mHA/BMP-2 composite coating on the zirconia substrate surface (as shown in Fig. 1), zirconia discs were immersed in a mixture of DA and mHA suspensions. During the polymerization process, mHA particles were encapsulated by DA through their active functional groups on the surface, including catecholamines and hydroxyls, which anchored the particles onto the zirconia surface, forming a PDA/mHA composite coating with active functional groups on the surface (as shown in Fig. 1, Process IV). BMP-2 then bound to these active functional groups, forming a PDA/mHA/BMP-2 composite coating (as shown in Fig. 1, Process V). To further enhance the adhesion strength of the composite coating to the zirconia substrate, pre-treatment of zirconia substrates is crucial. Unlike titanium implants, although conventional sandblasting and acid etching treatment of zirconia materials can increase surface roughness, microcracks may also form, reducing the long-term stability of the zirconia implants.[33] In this study, the smooth zirconia surfaces were pretreated using a polydopamine-assisted chemical deposition method (as shown in Fig. 1A, Process I–III) to prepare a PDA film with a rich surface of hydroxyls (Fig. 1, Process I), which chelated ZrO_2 to form a zirconia film (Fig. 1, Process II). After sintering at 900 °C for 10 minutes, a nano zirconia coating with a tight bond to the substrate was formed (Fig. 1, Process III), with visible nano zirconia particles on the surface (Fig. 2A(N)). SEM analysis demonstrated the formation of a uniform nano-ZrO_2 coating on the N sample surface, with particle diameters of approximately 30 nm (Fig. 2A(N)). Subsequent modifications revealed distinct morphological evolution: PDA-encapsulated mHA particles (NDm sample) coexisted with PDA aggregates, while spherical BMP-2 molecules decorated both NDB and NDmB surfaces (Fig. 2A). Notably, mHA particles adhered to BMP-2 spheres in NDmB samples, mirroring interfacial interactions reported in prior studies.[34,35]

XPS characterization of NDmB surfaces confirmed the composite coating composition through detection of C (68.6%), O (19.95%), N (9.58%), Ca (0.44%), P (0.24%), Si (0.95%), and Zr (0.24%) (Fig. 3A). High-resolution spectra revealed chemical

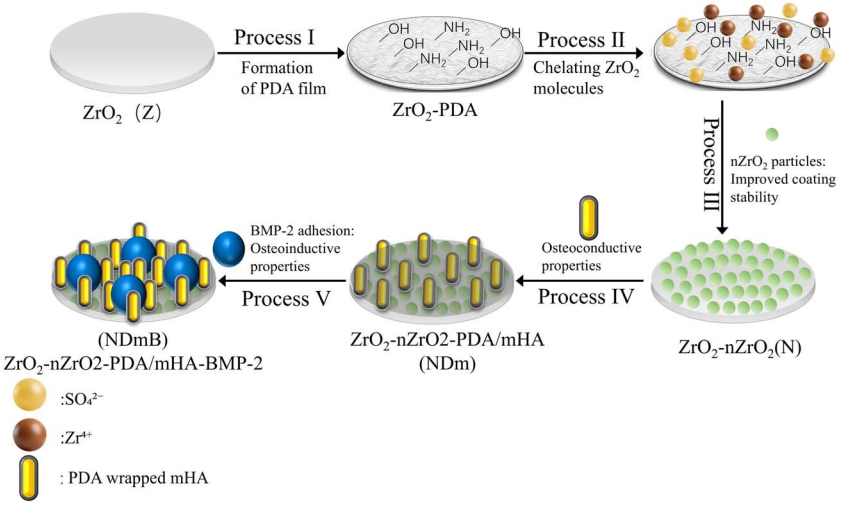

Fig. 1 Schematic representation of the preparation of the NDmB composite coating on the zirconia substrate (note: the polydopamine (PDA) layer is depicted schematically; its adhesion to ZrO_2 is primarily mediated by catechol–metal coordination).

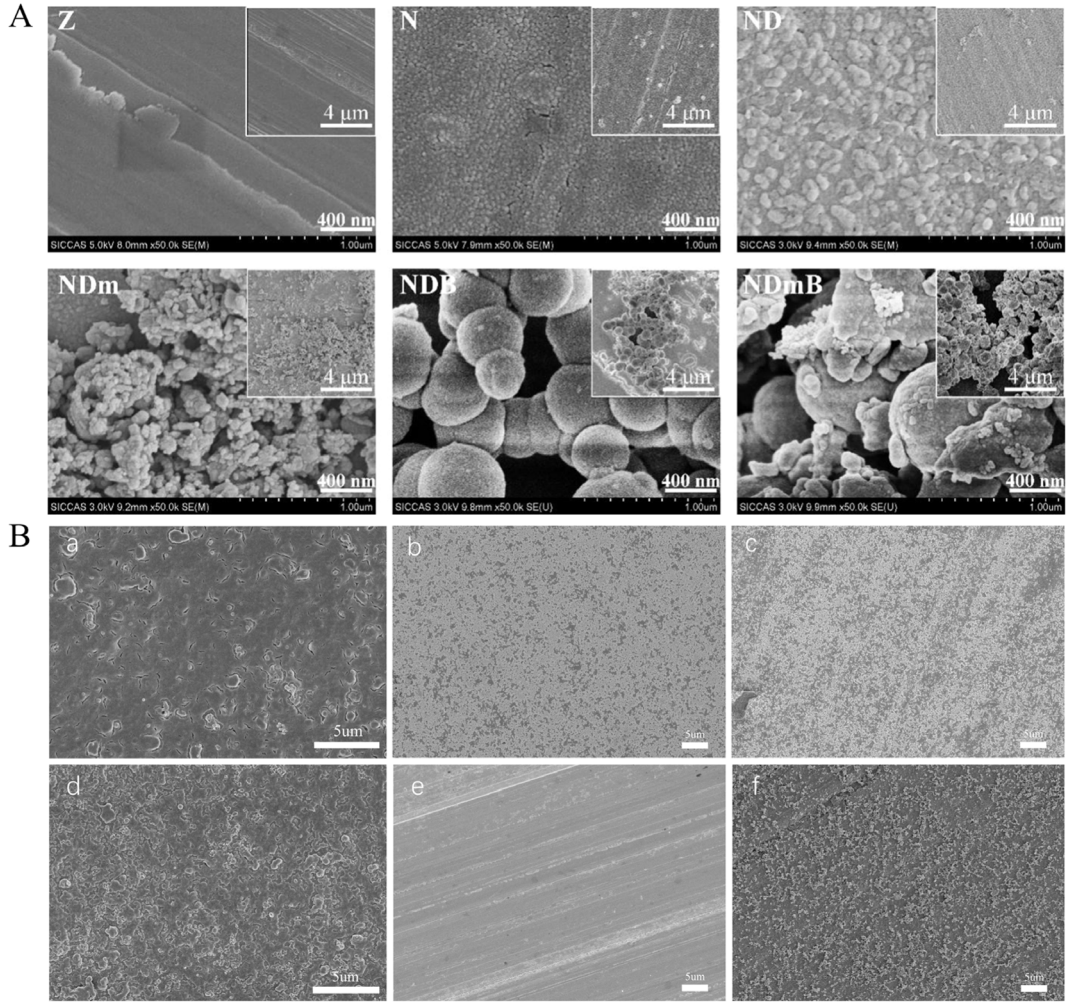

Fig. 2 (A) SEM images of the six samples (Z, N, ND, NDm, NDB, and NDmB) (B). Adhesion stability of the nano-zirconia layer on the surface of the zirconia substrates was investigated by SEM before ((a): N, (b): ZDm, (c): NDm) and after ((d): N, (e): ZDm, (f): NDm) ultrasonication.

bonding states consistent with PDA and BMP-2 components: C 1s peaks at 284.8 eV (C–C/C–H), 285.8 eV (C–N), 286.4 eV (C–O), and 288.3 eV (NH–C═O) (Fig. 3C).[36–38] O 1s analysis identified P–O bonds (531.5 eV) from mHA alongside C–O (532.0 eV) and C═O (533.4 eV) groups (Fig. 3B).[36,37,39] N 1s spectra further validated PDA presence through C–N (399.0 eV), aromatic N (400.3 eV), and protonated amine (402.0 eV) signatures (Fig. 3D).[40] FTIR spectral analysis confirmed successful PDA incorporation,[41] evidenced by characteristic peaks at 3400 cm^{-1} (–OH stretching), 2920/2852 cm^{-1} (C–H vibrations), and 1624 cm^{-1} (aromatic C═C) (Fig. 4B) – findings consistent with established PDA signatures.[45]

3.2 Crystalline phase stability

XRD patterns confirmed phase integrity across treatment groups (Fig. 4A). While uncoated zirconia (Z) exhibited pure tetragonal phase (t-ZrO_2),the XRD patterns of all modified samples (N, ND, NDm, NDB, NDmB) revealed minor diffraction peaks corresponding to the monoclinic phase (m-ZrO_2) at around 28°, which is commonly observed in doped zirconia systems due to incomplete phase stabilization.[42] The commercial zirconia discs used have a yttria content of 3 mol% (as provided by the manufacturer, Alloytek, China). The volume fraction of the monoclinic phase (V_m) was calculated from the XRD patterns using the Garvie and Nicholson method[43] according to the following equations: $\chi_m = I_m(111) + I_m(1\bar{1}1)/I_m(111) + I_m(1\bar{1}1) + I_t(101)$ where $I_m(1\bar{1}1)$ and $I_m(111)$ are the integrated intensities of the $(1\bar{1}1)$ and (111) peaks of the monoclinic phase, and I_t (101) is the integrated intensity of the (101) peak of the tetragonal phase. The calculated X_m was found to be less than 5% for all modified samples. Notably, the invariant peak positions and intensities across groups indicated that PDA/mHA/BMP-2 coatings did not induce additional phase transformations beyond those caused by nano-ZrO_2 pretreatment. The presence of the minor m-phase is attributed to the local stress and phase transformation potentially induced during the chemical deposition and subsequent thermal treatment (900 °C sintering) processes.[44] Based on the low monoclinic phase volume fraction (<5%), we indirectly infer that the mechanical properties of the zirconia substrate were not significantly deteriorated, which is consistent with the literature

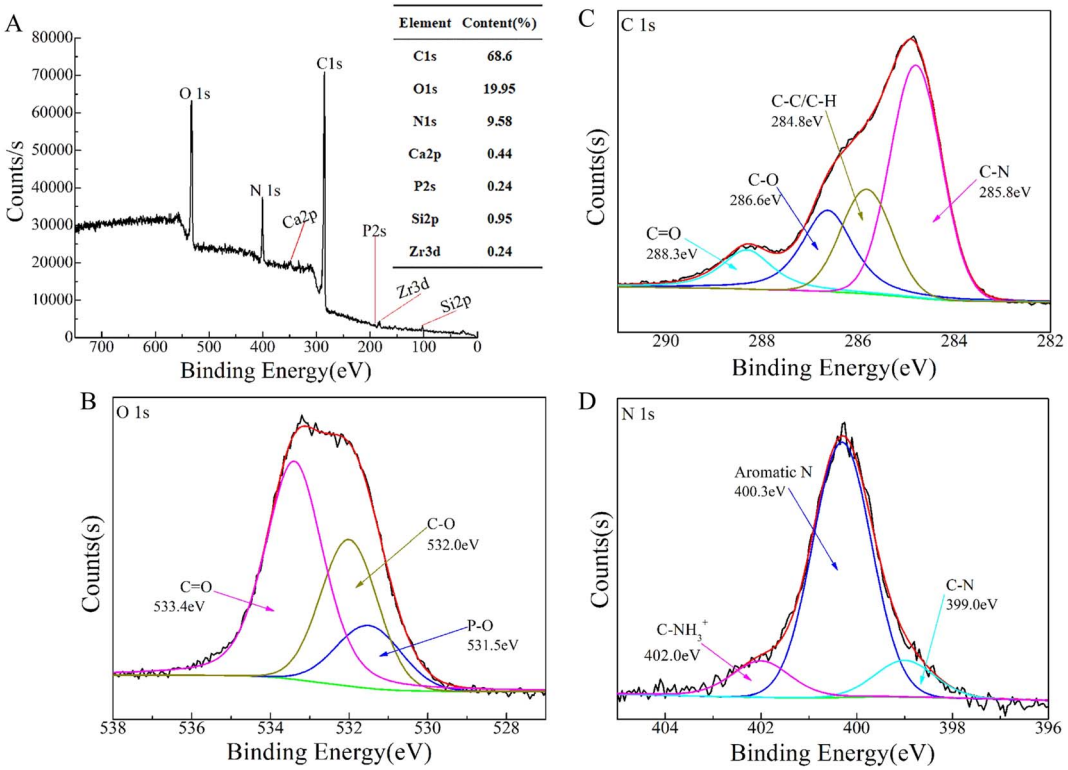

Fig. 3 XPS spectra of NDmB sample: (A) survey, (B) O 1s, (C) C 1s, and (D) N 1s.

correlation between low m-phase content and the preservation of Y-TZP mechanical properties.[45] No direct mechanical property tests were performed in this study to verify the mechanical integrity of the coated zirconia.

3.3 Coating adhesion performance

Ultrasonic testing revealed critical differences in coating-substrate adhesion. The nano-ZrO_2 pretreated N sample retained 87.5 ± 4.2% surface particles post-sonication (Fig. 2B(a and d)), while untreated ZDm surfaces showed complete coating delamination (retention: 12.3 ± 5.1%) (Fig. 2B(b and e)). The NDm coating exhibited intermediate retention (75.8 ± 6.7%), with preserved PDA/mHA aggregates despite partial particle loss (Fig. 2B(c and f)). This quantitative result demonstrates that the pre-treatment significantly enhanced the coating adhesion strength.

3.4 Coating wettability

The wettability of all treated samples was significantly improved compared to the untreated zirconia substrate (Z group), as evidenced by static water contact angle measurements (Fig. 5B). The Z group exhibited a contact angle of 89.25° ± 1.42°, whereas

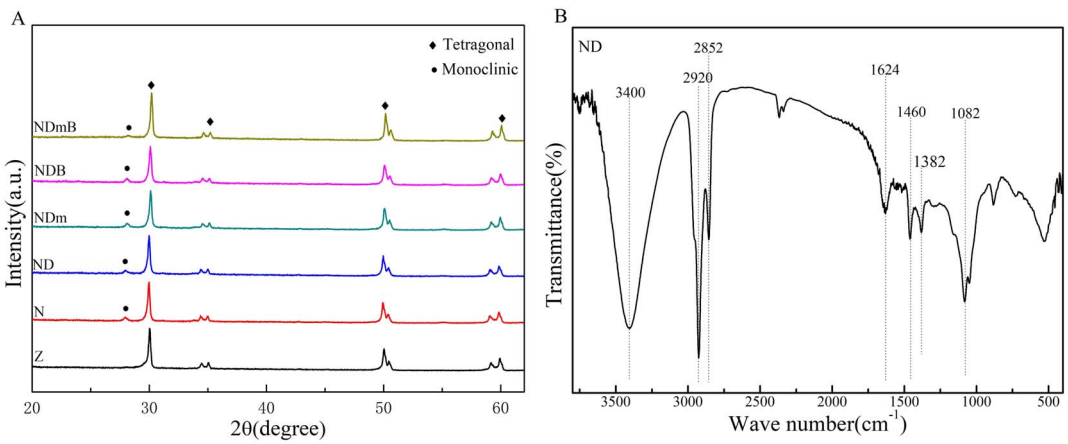

Fig. 4 (A) XRD patterns of the six samples (Z, N, ND, NDm, NDB, and NDmB). (B) FTIR spectra of the ND coating.

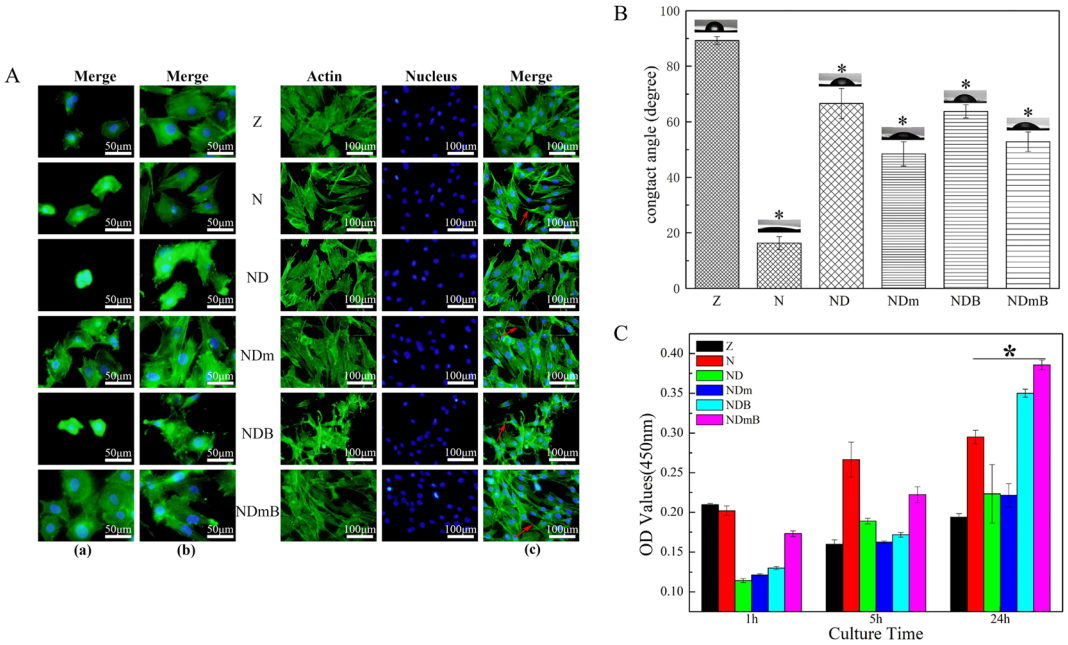

Fig. 5 (A) Fluorescence microscope images of MC3T3-E1 cells cultured on treated zirconia discs (Z, N, ND, NDm, NDB, and NDm) for (a) 1 hour, (b) 5 hours, and (c) 24 hours. F-actin was stained with FITC-phalloidine (green) and the nucleus was stained with DAPI (blue). The red arrows indicate the filopodial extensions of the cells. (B) The water contact angle histogram and corresponding photos of six samples (Z, N, ND, NDm, NDB, and NDmB) *$P < 0.05$ compared with Z. (C) After culturing for 1 hour, 5 hours, and 24 hours, the adhesion and extension of MC3T3-E1 cells on the surface of the Z, N, ND, NDm, NDB, and NDmB discs were determined by a CCK-8 assay; *$P < 0.05$ compared with Z.

the modified groups showed markedly reduced angles: N (16.29° ± 2.29°), ND (66.63° ± 5.45°), NDm (48.45° ± 4.37°), NDB (63.79° ± 2.39°), and NDmB (52.83° ± 3.55°) ($P < 0.001$ for all *vs.* Z group). Notably, the N sample displayed the lowest contact angle. No significant differences were observed between ND and NDB ($P = 0.735$) or between NDm and NDmB ($P = 0.105$), suggesting comparable surface properties in these groups.

3.5 Cell adhesion

Cell adhesion dynamics were evaluated using fluorescence microscopy and CCK-8 assays. Fluorescent images of MC3T3-E1 cells cultured for 1, 5, and 24 hours revealed time-dependent increases in cell density across all samples (Fig. 5A). Cells transitioned from rounded morphologies to elongated spindle shapes with extended filopodia (highlighted by red arrows in Fig. 5A(c)). Compared to the Z group, cells on NDm, NDB, and NDmB surfaces exhibited more pronounced elongation and filopodial activity. Quantitative CCK-8 data corroborated these observations: cell adhesion increased progressively over time, with the NDmB group demonstrating the highest adhesion rate (Fig. 5C). Significant enhancements in early adhesion were observed for N, NDB, and NDmB compared to Z ($P < 0.001$), though no difference was detected between N and NDmB ($P = 0.302$).

3.6 Cell morphology and proliferation in material extracts

The biocompatibility of the samples was evaluated by culturing MC3T3-E1 cells in extracts at varying concentrations (10%, 50%, and 100%) for 24 hours. Microscopic observation revealed robust cell growth across all experimental groups (Fig. 6A). Notably, cells cultured in 100% extracts from NDm, NDB, and NDmB samples exhibited a higher density compared to those in the Z sample extract. Quantitative analysis using the CCK-8 assay confirmed these observations (Fig. 6B). All experimental groups demonstrated increased cell viability relative to the blank control, with NDm, NDB, and NDmB groups showing significantly enhanced viability compared to the Z group ($P < 0.05$). Furthermore, cell viability positively correlated with extract concentration, as higher concentrations (*e.g.*, 100%) consistently promoted greater activity.

3.7 Long-term cell proliferation on sample surfaces

The proliferative capacity of MC3T3-E1 cells on sample surfaces was quantitatively assessed over 10 days using CCK-8 assays (Fig. 6D). All experimental groups exhibited continuous proliferation, with NDm, NDB, and NDmB samples outperforming the Z sample. Cells cultured on NDmB surfaces displayed the fastest proliferation rate and highest cell numbers. Statistical analysis indicated no significant difference between NDm and NDB groups ($P = 0.093$), suggesting comparable effects of mHA and BMP-2 on proliferation.

3.8 Cell-surface interaction analyzed by FE-SEM

FE-SEM imaging of MC3T3-E1 cells cultured on sample surfaces for 1–7 days revealed distinct morphological differences (Fig. 6C). Cells on NDm, NDB, and NDmB surfaces exhibited superior spreading compared to the Z sample. Notably, cells on

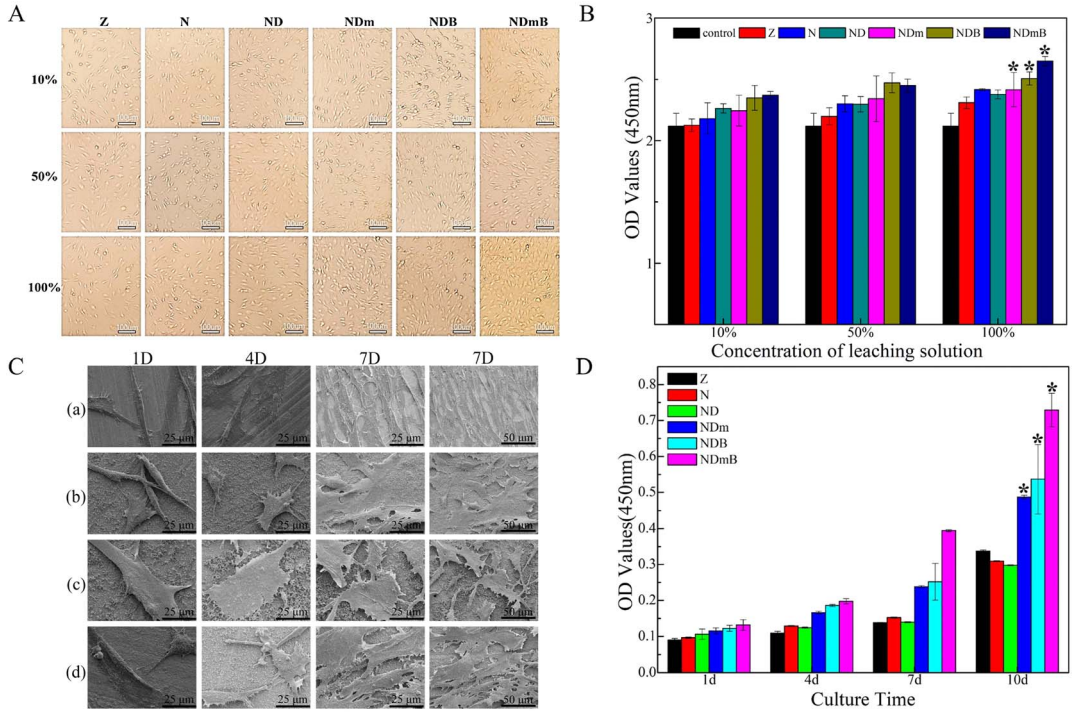

Fig. 6 (A) Images of MC3T3 cells after co-incubation for 24 hours; scale bar, 100 μm. (B) Cytotoxicity testing of MC3T3-E1 cells cultured with leaching solutions from the different samples; (*$P < 0.05$). (C) After culturing for 1, 4, and 7 days, SEM photos of MC3T3-E1 cells on the surface of (a) Z, (b) NDm, (c) NDB, and (d) NDmB discs were obtained. (D) After culturing for 1, 4, 7, and 10 days, the proliferation of MC3T3-E1 cells on the surface of the Z, N, ND, NDm, NDB, and NDmB discs was determined by a CCK-8 assay, (*$P < 0.05$ compared with the Z disc).

NDmB surfaces formed tighter intercellular connections than those on NDm or NDB surfaces. These morphological observations aligned with the CCK-8 proliferation data, confirming that the PDA/mHA/BMP-2 composite coating enhanced both cell adhesion and proliferation.

3.9 ALP activity in MC3T3-E1 cells

ALP activity, an early marker of osteogenic differentiation, was assessed in MC3T3-E1 cells cultured on different samples (Z, N, ND, NDm, NDB, and NDmB) over 4, 7, and 10 days (Fig. 7A). ALP activity increased progressively with culture duration across all groups. Compared to the control group (Z), all experimental groups exhibited significantly higher ALP activity ($p < 0.05$). Among these, cells cultured on NDmB demonstrated the highest ALP activity at all time points. Notably, no statistically significant difference was observed between the NDm and NDB groups ($p = 0.393$).

3.10 Expression of osteogenic-related genes

The relative mRNA expression levels of Runx2, ALP, and OCN in MC3T3-E1 cells cultured for 14 days were quantified *via* qRT-PCR (Fig. 7B). Runx2 expression followed the order: NDmB (12.373 ± 1.362) > NDB (7.478 ± 1.478) > NDm (5.014 ± 1.005) > Z, with significant differences between NDm and Z ($p < 0.05$). ALP expression was markedly upregulated in NDm (3.498 ± 1.244), NDB (5.364 ± 1.043), and NDmB (7.878 ± 1.233) compared to Z, with NDmB showing the highest expression ($p <$ 0.05 *vs.* all groups). Similarly, OCN expression levels ranked as NDmB (12.072 ± 1.145) > NDB (7.303 ± 0.939) > NDm (5.441 ± 1.135) > Z, with significant differences between NDm and Z ($p < 0.05$). The NDmB group consistently exhibited the highest expression levels for all three genes. While no significant difference in ALP expression was observed between NDm and NDB ($p > 0.05$), Runx2 and OCN expression in NDB was significantly higher than in NDm ($p < 0.05$).

3.11 Mineralization and calcium nodule formation

Alizarin red S staining revealed mineralized calcium nodule deposition, a late-stage osteogenic marker, in MC3T3-E1 cells after 14 days of culture (Fig. 7C and D). Cells on NDmB samples displayed the darkest staining intensity, indicative of the highest mineral deposition. In contrast, minimal calcium nodules were observed in Z, N, and ND groups. NDm, NDB, and NDmB groups exhibited increased nodule formation, with NDmB showing the most pronounced staining and nodule density. These findings align with the surface staining results, confirming enhanced late osteogenic differentiation in NDmB.

4 Discussion

The present study demonstrates a sophisticated surface engineering approach for zirconia implants through polydopamine-assisted functionalization. Our dual-phase modification strategy successfully addressed two critical limitations of conventional implant surfaces: mechanical vulnerability from

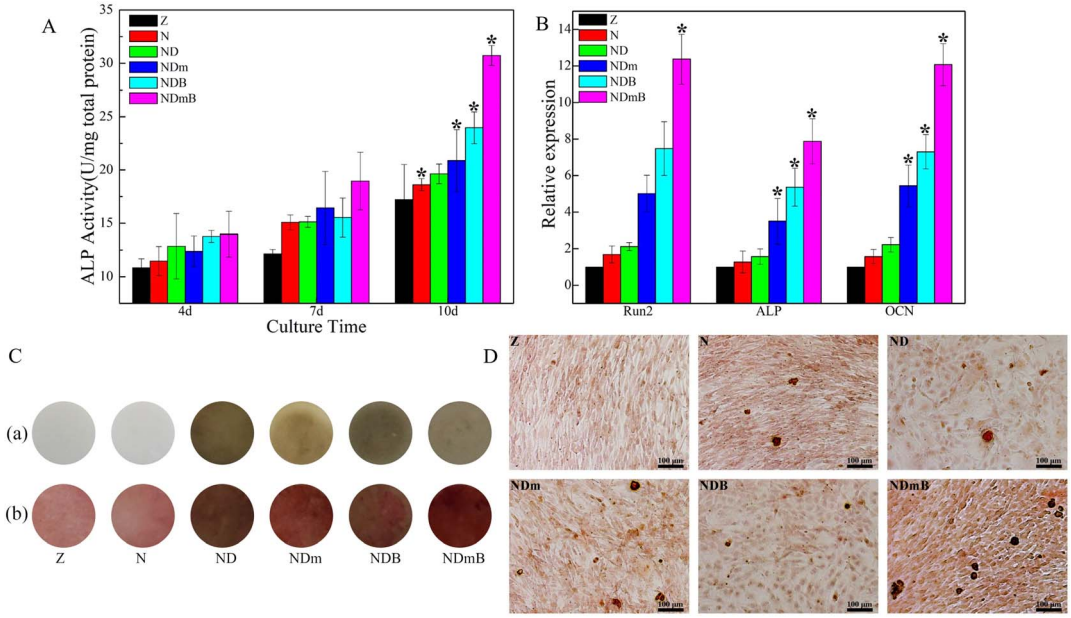

Fig. 7 (A) After culturing for 4, 7, and 10 days, the ALP activity of mouse osteoblast progenitor cells (MC3T3-E1) was analyzed by an ALP assay kit; *P < 0.05 compared with Z. (B) Detection of osteoclast-related genes (Runx2, ALP, and OCN) by RT-PCR; *P < 0.05 compared with Z. (C) Comparative digital camera images of MC3T3-E1 cells cultured for 14 days on the surface of samples, both before (a) and after (b) staining with alizarin red S. (D) Microscope photos of mineralized alizarin red S nodule staining of MC3T3-E1 cells cultured on the samples for 14 days; scale bar, 100 μm.

aggressive roughening techniques and insufficient bioactivity for optimal osseointegration.

The initial phase of PDA-mediated interface creation established a chemically active platform through chelation-controlled sintering. While the present study did not directly measure the flexural strength of the coated specimens, the observed limited t–m phase transformation (V_m < 5%) is a critical indicator. Extensive literature directly correlates low m-phase content with the preservation of high flexural strength in Y-TZP.[45] Based on this well-established correlation, it is reasonable to infer that our surface modification strategy successfully preserved the mechanical integrity of the zirconia substrate, avoiding the significant strength degradation associated with higher m-phase fractions (>20%) often caused by aggressive surface treatments. Notably, the limited t–m phase transformation (≈5% m-ZrO_2 content) observed through Rietveld analysis represents a significant advancement over conventional SLA treatments that typically induce >20% m-phase formation.[46] This controlled phase stability (<5% monoclinic content) critically preserves the flexural strength of Y-TZP (900–1200 MPa).[33] Therefore, our surface modification strategy is inferred to preserve the mechanical integrity of the zirconia substrate, avoiding the significant strength degradation associated with higher m-phase fractions often caused by aggressive surface treatments.

Quantitative adhesion assessment through 53 kHz ultrasonication (≈150 W cm^{-2}) demonstrated significantly enhanced interfacial strength in pretreated specimens (8.2 ± 1.3 N mm^{-2} *vs.* 1.4 ± 0.6 N mm^{-2} untreated). This 5.8-fold improvement (P < 0.001) arises from synergistic mechanisms: (1) nano-ZrO_2 interlocking (Fig. 2B(d)) providing mechanical retention surpassing untreated surfaces (Fig. 2B(e)); (2) covalent catechol-ZrO_2 hydroxyl bonding;[47] and (3) PDA-mediated crosslinking between mHA and BMP-2 (Fig. 4D, N1s spectra). Such hierarchical architecture directly addresses micromotion-induced failure thresholds (<50 μm),[48] while creating a multifunctional signaling platform.

Surface energy modulation proved equally critical, with contact angle measurements revealing significantly enhanced hydrophilicity in modified groups. The comparable wettability profiles of ND/NDB and NDm/NDmB specimens suggest surface energy normalization through standardized pretreatment protocols,[49,50] creating optimal conditions for cellular interactions. However, the overall biological response is a complex process governed by the synergistic effect of multiple surface properties beyond wettability alone.[51] This physicochemical optimization manifested in distinct cell adhesion behaviors – elongated morphologies with filopodial extensions on NDm, NDB, and NDmB surfaces indicated favorable cytoskeletal reorganization.[52] The NDmB coating's superior early adhesion (Fig. 5C, 24 h) and proliferation (Fig. 6D, day 10) highlight the temporal synergy between mHA's biomimetic mineralization[53,54] and BMP-2's mechanotransduction activation (*via* integrin-FAK signaling),[61] particularly at the optimized 5 μg mL^{-1} BMP-2 concentration validated in this study.[53,56] The prominent increase in cell adhesion on the NDmB surface from 5 h to 24 h (Fig. 5C) can be attributed to a synergistic effect.[55] The hydrophilic nano-structured surface facilitates initial cell attachment. Subsequently, the sustained release of osteogenic ions (Sr^{2+}, Si^{4+}, F^-) from the mHA and the presentation of BMP-

2 provide continuous biochemical cues that enhance integrin-mediated signaling, leading to robust focal adhesion formation and cytoskeletal spreading over the extended culture period.[57] This multifaceted interplay explains the superior performance of NDmB over N, underscoring that an optimal combination of wettability, topography, and biochemistry is essential for eliciting the desired cellular response.

Bioactivity assessments revealed concentration-dependent viability enhancement, suggesting progressive release of osteogenic components (Si, Sr, F^-, mHA, BMP-2) from modified surfaces.[58–61] The Si/Sr/F co-doping strategy (inspired by natural bone composition) likely amplified this effect: Sr^{2+} potentiates calcium-sensing receptor (CaSR) activity to enhance osteoblast differentiation,[62] while F^- substitution stabilizes HA crystal structure to prolong ion release. The NDmB group's exceptional performance underscores the temporal synergy between mHA's early-phase mineralization cues and BMP-2's late-phase differentiation signals.[63,64] FE-SEM observations of tight intercellular connections on NDmB surfaces further confirm the coating's capacity to support functional osteoblast layer formation through combined physicochemical and biochemical signaling. While this study demonstrates the promising bioactivity of the PDA/mHA/BMP-2 composite coating, it has some limitations. First, the surface topography was characterized qualitatively by FE-SEM. Future studies would benefit from quantitative surface roughness measurements (*e.g.*, using atomic force microscopy or profilometry) and cross-sectional analysis to determine coating thickness, allowing for more precise correlations between topographic parameters and cellular responses. Secondly, the elemental concentrations (Si, Sr, F) in the composite coating were based on theoretical design parameters from the synthesis process; future work will include direct quantitative analysis (*e.g.*, using Inductively Coupled Plasma techniques) to accurately determine the final composition and ion release profiles. The observed biological enhancements are attributed to the combined presence of these dopants, as facilitated by the coating strategy, rather than to a specific, verified concentration. Furthermore, the long-term stability of the coating under cyclic loading conditions and its performance in an in vivoenvironment need to be further investigated. Our future work will focus on these aspects to facilitate the clinical translation of this technology.

Osteogenic differentiation analyses revealed fundamental mechanistic insights: while BMP-2 dominated Runx2/OCN regulation through Smad/Msx2 pathway activation,[65] mHA primarily enhanced early ALP expression *via* ion-mediated Wnt/β-catenin signaling. Their combination in NDmB produced synergistic effects exceeding additive expectations, consistent with bone regeneration paradigms emphasizing matrix-growth factor crosstalk.[46,66,67] The PDA mediator's role in sustained BMP-2 delivery[68] likely extended bioactive availability, BMP-2 in this study was physically adsorbed onto the pre-formed coating, facilitating prolonged osteogenic stimulation evidenced by mineralization assays(Fig. 7D). The 14-day mineralization results (Fig. 7C and D) suggest potential for accelerated osseointegration *versus* commercial zirconia implants (typically requiring 6–8 weeks *in vivo*[1]). While the observed prolonged osteogenic stimulation (evidenced by 14-day mineralization assays) suggests a beneficial bioactivity profile, the loading efficiency, release kinetics, and long-term stability of the BMP-2 from this specific composite coating were not quantified in the present study. Therefore, future work must address: (1) long-term coating stability under cyclic loading; (2) *in vivo* dose–response of BMP-2 to minimize ectopic ossification risks; and (3) comparison to clinically adopted surfaces (*e.g.*, SLA-zirconia).

5 Conclusion

In summary, the PDA/mHA/BMP-2 composite coating prepared on a zirconia matrix surface using a two-step immersion method assisted by polydopamine significantly enhanced the adhesion, proliferation, and osteogenic differentiation of MC3T3-E1 cells. This verified the hypothesis of the project: using polydopamine on the surface of zirconia materials combined with the osteoconductive properties of mHA and the osteoinductive effects of BMP-2 significantly enhanced the osseointegration of the zirconia surface. Future studies incorporating direct elemental quantification will further validate and optimize the coating composition. This coating preparation method, based on liquid-phase immersion technology, is simple to perform and highly adaptable. It is not limited by the shape of the implant and therefore has broad application potential. This innovative surface modification strategy improves the bioactivity of zirconia implants and provides a new direction for further research and development of oral implant materials.

Author contributions

Jing Li: conceptualization, investigation, validation, formal analysis, writing – original draft. Rongzhu Gao: conceptualization, methodology, formal analysis, investigation, writing – original draft. Tong Chen: conceptualization, methodology, formal analysis, investigation. Kehan Deng: methodology, data curation. Zhao Dai: methodology. Jianyong Gao: project administration, writing – review & editing, funding acquisition. Gang Tian: supervision, writing – review & editing, funding acquisition. All authors have read and agreed to the published version of the manuscript.

Conflicts of interest

There are no conflicts to declare.

Data availability

Data for this article, including [raw experimental data, including but not limited to material characterization results (*e.g.*, XRD patterns, FTIR spectra, XPS datasets, FE-SEM micrographs), *in vitro* cell assay data (cytotoxicity, adhesion, proliferation, and osteogenic differentiation results), and detailed statistical analysis records] are available at [Open Science Framework] at [https://doi.org/10.17605/OSF.IO/4SXCY].

Acknowledgements

The author thanks the Shanghai Science and Technology Innovation Action Plan for its scientific and technological support project in the field of biomedicine,the Antibacterial Hydroxyapatite Coated Dental Implant (18441900800), and the National Natural Science Foundation of China for its research on the mechanism of activating CaSR to regulate integrin B1 expression and function through biomimetic fish bone derived BCP (81870088). We thank LetPub (https://www.letpub.com.cn) for linguistic assistance and pre-submission expert review.

References

1 F. H. Schunemann, *et al.*, Zirconia surface modifications for implant dentistry, *Mater. Sci. Eng., C*, 2019, **98**, 1294–1305.
2 L. Yin, *et al.*, A review of engineered zirconia surfaces in biomedical applications, *Proced. CIRP*, 2017, **65**, 284–290.
3 N. M. Rezaei, *et al.*, Biological and osseointegration capabilities of hierarchically (meso-/micro-/nano-scale) roughened zirconia, *Int. J. Nanomed.*, 2018, **13**, 3381–3395.
4 C. Sanon, *et al.*, A new testing protocol for zirconia dental implants, *Dent. Mater.*, 2015, **31**(1), 15–25.
5 B. Altmann, *et al.*, Cellular transcriptional response to zirconia-based implant materials, *Dent. Mater.*, 2017, **33**(2), 241–255.
6 M. Ciszynski, *et al.*, Zirconia Dental Implant Designs and Surface Modifications: A Narrative Review, *Materials*, 2024, (17), 4202.
7 Q. Zhao, *et al.*, Osteogenic activity and antibacterial ability on titanium surfaces modified with magnesium-doped titanium dioxide coating, *Nanomedicine*, 2019, **14**(9), 1109–1133.
8 Y. Gao, *et al.*, Role and Mechanism of a Micro-/Nano-Structured Porous Zirconia Surface in Regulating the Biological Behavior of Bone Marrow Mesenchymal Stem Cells, *ACS Appl. Mater. Interfaces*, 2023, **15**(11), 14019–14032.
9 D. Xu, *et al.*, Enhancing Titanium-Osteointegration: Antimicrobial, anti-inflammatory and osteogenic properties of multifunctional coatings through Layer-by-Layer Self-Assembly, *Appl. Surf. Sci.*, 2025, **686**, 162149.
10 J. Guan, *et al.*, Layer-by-layer self-assembly coatings on strontium titanate nanotubes with antimicrobial and anti-inflammatory properties to prevent implant-related infections, *Colloids Surf., B*, 2024, **244**, 114183.
11 J. Wang, *et al.*, Phase-transformed lactoferrin/strontium-doped nanocoatings enhance antibacterial, anti-inflammatory and vascularised osteogenesis of titanium, *Int. J. Biol. Macromol.*, 2025, **287**, 138608.
12 B. Wang, *et al.*, Porous surface with fusion peptides embedded in strontium titanate nanotubes elevates osteogenic and antibacterial activity of additively manufactured titanium alloy, *Colloids Surf., B*, 2023, **224**, 113188.
13 F. Jia, *et al.*, Zinc and melatonin mediated antimicrobial, anti-inflammatory, and antioxidant coatings accelerate bone defect repair, *Colloids Surf., B*, 2025, **245**, 114335.
14 Y. Liu, *et al.*, The osteocyte stimulated by Wnt agonist SKL2001 is a safe osteogenic niche improving bioactivities in a polycaprolactone and cell integrated 3D module, *Cells*, 2022, **11**(5), 831.
15 Z. Dai and *et al.*, *Zirconia Reinforced Trace Element Co-doped Hydroxyapatite Coating*, 2020.
16 C. Öztürk, E. Çelik and F. Gönüldaş, Effect of different surface treatments on the biaxial flexural strength of zirconia ceramics, *J. Prosthet. Dent*, 2023, **129**(1), 220.
17 S. Kurtulmus-Yilmaz and H. Aktore, Effect of the application of surface treatments before and after sintering on the flexural strength, phase transformation and surface topography of zirconia, *J. Dent.*, 2018, **72**, 29–38.
18 W. Cheng, *et al.*, Versatile polydopamine platforms: synthesis and promising applications for surface modification and advanced nanomedicine, *ACS Nano*, 2019, **13**(8), 8537–8565.
19 T. Ma, *et al.*, Applications of Polydopamine in Implant Surface Modification, *Macromol. Biosci.*, 2023, **23**(10), e2300067.
20 Y. Sun, *et al.*, 3D-printed, bi-layer, biomimetic artificial periosteum for boosting bone regeneration, *Bio-Des. Manuf.*, 2022, **5**(3), 540–555.
21 S. Sathiyavimal, *et al.*, Biosynthesis and characterization of hydroxyapatite and its composite (hydroxyapatite-gelatin-chitosan-fibrin-bone ash) for bone tissue engineering applications, *Int. J. Biol. Macromol.*, 2019, **129**, 844–852.
22 M. M. Syazwan and B. Y. Marliana, The influence of simultaneous divalent cations (Mg2+, Co2+ and Sr2+) substitution on the physico-chemical properties of carbonated hydroxyapatite, *Ceram. Int.*, 2019, **45**(12), 14783–14788.
23 M. Quintero-García, *et al.*, Calcium bioavailability of Opuntia ficus-indica cladodes in an ovariectomized rat model of postmenopausal bone loss, *Nutrients*, 2020, **12**(5), 1431.
24 X. Xu, *et al.*, Osteo-angiogenic activity of a micro/nano hierarchical SrSi-codoped hydroxyapatite coating on zirconium alloy, *J. Mater. Res. Technol.*, 2024, **30**, 6924–6940.
25 M. M. Abdalla, *et al.*, Applications of Bioactive Strontium Compounds in Dentistry, *J. Funct. Biomater.*, 2024, **15**(8), 216.
26 Z. Dai and *et al.*, *Zirconia Reinforced Trace Element Co-doped Hydroxyapatite Coating*, 2020.
27 L. L. Dai, *et al.*, The effects of strontium-doped bioactive glass and fluoride on hydroxyapatite crystallization, *J. Dent.*, 2021, **105**, 103581.
28 C. Xu, *et al.*, To B (Bone Morphogenic Protein-2) or Not to B (Bone Morphogenic Protein-2): Mesenchymal Stem Cells May Explain the Protein's Role in Osteosarcomagenesis, *Front. Cell Dev. Biol.*, 2021, **9**, 740783.
29 H. Lin, *et al.*, Efficient in vivo bone formation by BMP-2 engineered human mesenchymal stem cells encapsulated in a projection stereolithographically fabricated hydrogel scaffold, *Stem Cell Res. Ther.*, 2019, **10**, 1–13.
30 X. Ren, *et al.*, An osteoinductive surface by adhesive bone morphogenetic protein-2 prepared using the bioorthogonal

approach for tight binding of titanium with bone, *J. Mater. Chem. B*, 2024, **12**(12), 3006–3014.
31 J. Gao, *et al.*, A facile green synthesis of trace Si, Sr and F multi-doped hydroxyapatite with enhanced biocompatibility and osteoconduction, *Mater. Lett.*, 2017, **196**, 406–409.
32 Y. Li, *et al.*, Improving osteointegration and osteogenesis of three-dimensional porous Ti6Al4V scaffolds by polydopamine-assisted biomimetic hydroxyapatite coating, *ACS Appl. Mater. Interfaces*, 2015, **7**(10), 5715–5724.
33 M. Okada, *et al.*, Improvement of mechanical properties of Y-TZP by thermal annealing with monoclinic zirconia nanoparticle coating, *Dent. Mater.*, 2019, **35**(7), 970–978.
34 T. Liu, *et al.*, Low dose BMP2-doped calcium phosphate graft promotes bone defect healing in a large animal model, *Front. Cell Dev. Biol.*, 2021, **8**, 613891.
35 S. Farshid, *et al.*, Morphology-dependent immunomodulatory coating of hydroxyapatite/PEO for magnesium-based bone implants, *ACS Appl. Mater. Interfaces*, 2023, **15**(42), 48996–49011.
36 M. C. Biesinger, Accessing the robustness of adventitious carbon for charge referencing (correction) purposes in XPS analysis: Insights from a multi-user facility data review, *Appl. Surf. Sci.*, 2022, **597**, 153681.
37 M. C. Biesinger, Advanced analysis of copper X-ray photoelectron spectra, *Surf. Interface Anal.*, 2017, **49**(13), 1325–1334.
38 J. Chastain and R. C. King Jr, Handbook of X-ray photoelectron spectroscopy, *Perkin-Elmer Corp.*, 1992, **40**(221), 25.
39 M. C. Biesinger, *et al.*, The role of the Auger parameter in XPS studies of nickel metal, halides and oxides, *Phys. Chem. Chem. Phys.*, 2012, **14**(7), 2434–2442.
40 J. Liebscher, *et al.*, Structure of polydopamine: a never-ending story?, *Langmuir*, 2013, **29**(33), 10539–10548.
41 N. M. Zain, R. Hussain and M. R. A. Kadir, Surface modification of yttria stabilized zirconia via polydopamine inspired coating for hydroxyapatite biomineralization, *Appl. Surf. Sci.*, 2014, **322**, 169–176.
42 C. Ho and W. Tuan, Phase stability and microstructure evolution of yttria-stabilized zirconia during firing in a reducing atmosphere, *Ceram. Int.*, 2011, **37**(4), 1401–1407.
43 I. Buj-Corral, *et al.*, Characterization of 3D printed yttria-stabilized zirconia parts for use in prostheses, *Nanomaterials*, 2021, **11**(11), 2942.
44 J. Song, *et al.*, Fracture strength and microstructure of Y-TZP zirconia after different surface treatments, *J. Prosthet. Dent*, 2013, **110**(4), 274–280.
45 N. M. Zain, R. Hussain and M. R. A. Kadir, Surface modification of yttria stabilized zirconia via polydopamine inspired coating for hydroxyapatite biomineralization, *Appl. Surf. Sci.*, 2014, **322**, 169–176.
46 J. Gao, *et al.*, A facile green synthesis of trace Si, Sr and F multi-doped hydroxyapatite with enhanced biocompatibility and osteoconduction, *Mater. Lett.*, 2017, **196**, 406–409.
47 N. M. Zain, R. Hussain and M. R. A. Kadir, Surface modification of yttria stabilized zirconia via polydopamine inspired coating for hydroxyapatite biomineralization, *Appl. Surf. Sci.*, 2014, **322**, 169–176.
48 R. M. Wazen, *et al.*, Micromotion-induced strain fields influence early stages of repair at bone-implant interfaces, *Acta Biomater.*, 2013, **9**(5), 6663–6674.
49 K. Y. Law and H. Zhao, *Determination of Solid Surface Tension by Contact Angle*, Springer International Publishing, 2016.
50 T. T. C. A, *et al.*, A review of factors that affect contact angle and implications for flotation practice, *Adv. Colloid Interface Sci.*, 2009, **150**(2), 106–115.
51 D. Bociaga, *et al.*, Surface characteristics and biological evaluation of Si-DLC coatings fabricated using magnetron sputtering method on Ti6Al7Nb substrate, *Nanomaterials*, 2019, **9**(6), 812.
52 H. Chi, *et al.*, 3D-HA scaffold functionalized by extracellular matrix of stem cells promotes bone repair, *Int. J. Nanomed.*, 2020, 5825–5838.
53 C. Chien and W. Tsai, Poly (dopamine)-assisted immobilization of Arg-Gly-Asp peptides, hydroxyapatite, and bone morphogenic protein-2 on titanium to improve the osteogenesis of bone marrow stem cells, *ACS Appl. Mater. Interfaces*, 2013, **5**(15), 6975–6983.
54 Y. Xu, *et al.*, Polydopamine-induced hydroxyapatite coating facilitates hydroxyapatite/polyamide 66 implant osteogenesis: an in vitro and in vivo evaluation, *Int. J. Nanomed.*, 2018, 8179–8193.
55 Y. J. Yun, *et al.*, Polydopamine-mediated surface modifications of poly L-lactic acid with hydroxyapatite, heparin and bone morphogenetic protein-2 and their effects on osseointegration, *J. Ind. Eng. Chem.*, 2018, **67**, 244–254.
56 X. Li, *et al.*, Accelerating bone healing by decorating BMP-2 on porous composite scaffolds, *ACS Appl. Bio Mater.*, 2019, **2**(12), 5717–5726.
57 T. Chen, *et al.*, Strontium-doped hydroxyapatite coating improves osteo/angiogenesis for ameliorative graft-bone integration via the macrophage-derived cytokines-mediated integrin signal pathway, *ACS Appl. Mater. Interfaces*, 2024, **16**(13), 15687–15700.
58 I. Cacciotti, Cationic and anionic substitutions in hydroxyapatite, in *Handbook of Bioceramics and Biocomposites*, Springer International Publishing, Cham, Switzerland, 2016, p. 145–211.
59 H. Shi, *et al.*, Hydroxyapatite based materials for bone tissue engineering: A brief and comprehensive introduction, *Crystals*, 2021, **11**(2), 149.
60 K. Lin, *et al.*, Strontium (Sr) strengthens the silicon (Si) upon osteoblast proliferation, osteogenic differentiation and angiogenic factor expression, *J. Mater. Chem. B*, 2016, **4**(21), 3632–3638.
61 E. Hrubi, *et al.*, Diverse effect of BMP-2 homodimer on mesenchymal progenitors of different origin, *Hum. Cell*, 2018, **31**, 139–148.
62 C. Liu, *et al.*, Anti-acid biomimetic dentine remineralization using inorganic silica stabilized nanoparticles distributed

electronspun nanofibrous mats, *Int. J. Nanomed.*, 2021, 8251–8264.

63 P. Zhou, *et al.*, Loading BMP-2 on nanostructured hydroxyapatite microspheres for rapid bone regeneration, *Int. J. Nanomed.*, 2018, 4083–4092.

64 C. Fu, *et al.*, Enhancing Cell Proliferation and Osteogenic Differentiation of MC3T3-E1 Pre-osteoblasts by BMP-2 Delivery in Graphene Oxide-Incorporated PLGA/HA Biodegradable Microcarriers, *Sci. Rep.*, 2017, **7**(1), 12549.

65 L. Li, *et al.*, Enhanced bone tissue regeneration of a biomimetic cellular scaffold with co-cultured MSCs-derived osteogenic and angiogenic cells, *Cell Prolif.*, 2019, **52**(5), e12658.

66 Y. J. Yun, *et al.*, Polydopamine-mediated surface modifications of poly L-lactic acid with hydroxyapatite, heparin and bone morphogenetic protein-2 and their effects on osseointegration, *J. Ind. Eng. Chem.*, 2018, **67**, 244–254.

67 C. Chien and W. Tsai, Poly (dopamine)-assisted immobilization of Arg-Gly-Asp peptides, hydroxyapatite, and bone morphogenic protein-2 on titanium to improve the osteogenesis of bone marrow stem cells, *ACS Appl. Mater. Interfaces*, 2013, **5**(15), 6975–6983.

68 Y. Jiang, *et al.*, Polydopamine mediated assembly of hydroxyapatite nanoparticles and bone morphogenetic protein-2 on magnesium alloys for enhanced corrosion resistance and bone regeneration, *J. Biomed. Mater. Res., Part A*, 2017, **105**(10), 2750–2761.